Nanoelectronics and Its New Materials – A NEW ERA OF NANOSCIENCE

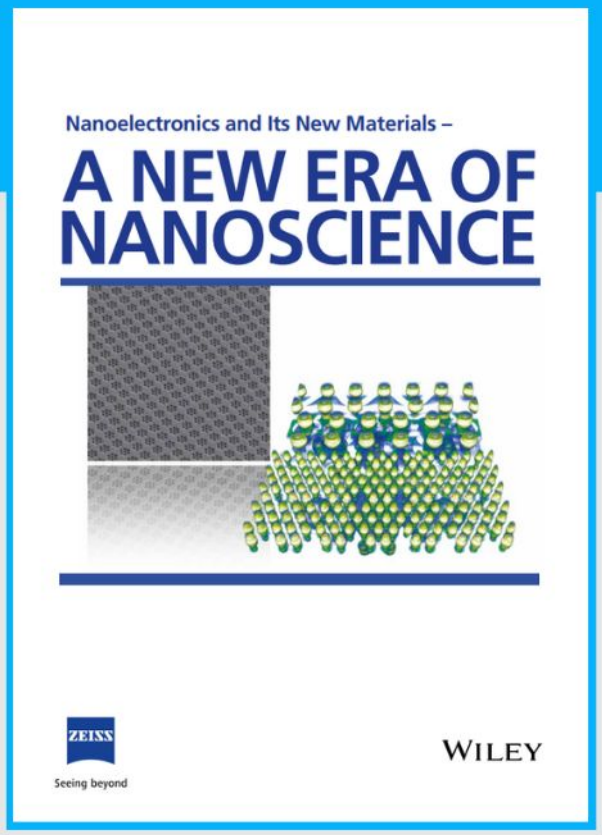

Discover the recent advances in electronics research and fundamental nanoscience.

Nanotechnology has become the driving force behind breakthroughs in engineering, materials science, physics, chemistry, and biological sciences. In this compendium, we delve into a wide range of novel applications that highlight recent advances in electronics research and fundamental nanoscience. From surface analysis and defect detection to tailored optical functionality and transparent nanowire electrodes, this eBook covers key topics that will revolutionize the future of electronics.

To get your hands on this valuable resource and unleash the power of nanotechnology, simply download the eBook now. Stay ahead of the curve and embrace the future of electronics with nanoscience as your guide.

ZEISS

Seeing beyond

WILEY

Check for updates

NANO · MICRO small
www.small-journal.com

Vapor-Phase Synthesis of Molecularly Imprinted Polymers on Nanostructured Materials at Room-Temperature

Elisabetta Mazzotta, Tiziano Di Giulio, Stefano Mariani, Martina Corsi, Cosimino Malitesta, and Giuseppe Barillaro**

Molecularly imprinted polymers (MIPs) have recently emerged as robust and versatile artificial receptors. MIP synthesis is carried out in liquid phase and optimized on planar surfaces. Application of MIPs to nanostructured materials is challenging due to diffusion-limited transport of monomers within the nanomaterial recesses, especially when the aspect ratio is >10. Here, the room temperature vapor-phase synthesis of MIPs in nanostructured materials is reported. The vapor phase synthesis leverages a >1000-fold increase in the diffusion coefficient of monomers in vapor phase, compared to liquid phase, to relax diffusion-limited transport and enable the controlled synthesis of MIPs also in nanostructures with high aspect ratio. As proof-of-concept application, pyrrole is used as the functional monomer thanks to its large exploitation in MIP preparation; nanostructured porous silicon oxide ($PSiO_2$) is chosen to assess the vapor-phase deposition of PPy-based MIP in nanostructures with aspect ratio >100; human hemoglobin (HHb) is selected as the target molecule for the preparation of a MIP-based $PSiO_2$ optical sensor. High sensitivity and selectivity, low detection limit, high stability and reusability are achieved in label-free optical detection of HHb, also in human plasma and artificial serum. The proposed vapor-phase synthesis of MIPs is immediately transferable to other nanomaterials, transducers, and proteins.

1. Introduction

Over the last decade, the molecular imprinting technique[1–6] has emerged as a robust and versatile tool for the preparation of artificial receptors for sensing and medical applications, the so-called molecularly imprinted polymers (MIPs). The increasing interest in MIPs relies on their ability to act as the synthetic alternative to biological receptors, keeping the high selectivity of the latter, yet featuring higher stability, lower cost, and synthesis adaptable to any target analyte.[7–9] MIPs are obtained by polymerization of functional monomer(s) in the presence of the target analyte, i.e., the template molecule, whose subsequent removal leaves binding cavities in the polymer network retaining shape, size, and functionality of the template.[10–12]

Integration of MIPs on the transducer surface remains a key issue for sensing applications, especially when nanostructured materials come into play.[5,6,13,14] Stable anchoring and controlled thickness are sought to improve sensor stability and reusability, as well as to provide accessible binding sites enabling rapid rebinding of the target analyte.[15–19]

Strategies for MIP deposition are carried out in liquid phase and have been mostly optimized on planar surfaces, so that their application to nanostructured materials remains challenging. Major challenges come from diffusion-limited transport of monomers within the nanostructure recesses/pores that leads to a growth rate of the MIP film that is uneven from top to bottom, especially when the aspect-ratio of the nanostructures is beyond 10, resulting in a not controlled and/or not uniform coating of the inner material surface over depth.[20–22] This generates a bottleneck effect at the recess/pore inlet as the deposition progresses, further restricting access of molecules to the inner part of the nanostructure and eventually leading to complete recess/pore blockage.

Surface initiated controlled/living polymerization, including iniferter polymerization, and dopamine polymerization have been used to date for the MIP synthesis on low and high aspect-ratio nanostructures,[23–28] namely, nanoparticles[29–32] and nanoporous scaffolds.[20–22,33] Nonetheless, the scarce control of the liquid-phase polymerization kinetics within the nanoporous material leads to the complete filling of the pores with polymer, precluding the formation of a polymer film with controlled thickness on the inner pore surface. Thus, removal of the template molecules–anchored to the inner surface of the nanopores–after polymer deposition requires the full etching of

E. Mazzotta, T. Di Giulio, C. Malitesta
Laboratory of Analytical Chemistry
Department of Biological and Environmental Sciences and Technologies (Di.S.Te.B.A.)
University of Salento
via Monteroni, Lecce 73100, Italy
E-mail: elisabetta.mazzotta@unisalento.it
S. Mariani, M. Corsi, G. Barillaro
Information Engineering Department
University of Pisa
via G. Caruso 16, Pisa 56122, Italy
E-mail: giuseppe.barillaro@unipi.it

The ORCID identification number(s) for the author(s) of this article can be found under https://doi.org/10.1002/smll.202302274

© 2023 The Authors. Small published by Wiley-VCH GmbH. This is an open access article under the terms of the Creative Commons Attribution License, which permits use, distribution and reproduction in any medium, provided the original work is properly cited.

DOI: 10.1002/smll.202302274

the hosting material–which cannot be used as the transducer–and free-standing MIP nanofilaments floating in the solution are achieved. A preliminary attempt to prepare MIPs by initiated chemical vapor deposition carried out at 280 °C in vacuum[33] led to similar results. In this case, the very high deposition temperature further prevents application to biomolecules as the template/target, which are damaged during the MIP preparation. Recently, novel imprinting schemes based on epitope-oriented surface imprinting combined with the use of silylating monomers have demonstrated to enable MIP synthesis with high targeting capability on several coreless and core-shell nanoparticles but not on high aspect ratio nanostructures.[34–36]

Thus, a general approach for the facile integration of MIPs with nanomaterials regardless of their aspect ratio that guarantees thickness control, homogeneous coating, good adhesion, and proper binding site exposure without sacrificial etching of the nanomaterial itself is of key importance for further extending application of MIPs to nanostructured (bio)sensing and nanomedicine, among others.

Here, we report on the synthesis of MIPs by vapor-phase polymerization at room temperature and atmospheric pressure as an effective alternative route to standard liquid-phase polymerization to control the preparation of MIPs in nanostructured materials, regardless of their aspect ratio. As a proof-of-concept application, we leverage the room-temperature vapor-phase synthesis of a PPy-based MIP within a nanostructured porous silicon oxide ($PSiO_2$) optical transducer for the fabrication and assessment of a MIP-based sensor. $PSiO_2$ is chosen as a difficult to coat nanostructured material for MIP deposition to prove the performance of the vapor-phase polymerization compared to common liquid-phase polymerization in high aspect-ratio (about 100) nanomaterials.[37–40] $PSiO_2$ acts not only as nanostructured scaffold but also as optical transducer thus demonstrating the advantage of the vapor-phase approach enabling nanostructured MIP synthesis and integration with the transducer in a single step with no need of additional steps for scaffold removal and/or integration with the transducer, contrarily to what observed in other imprinting approaches for MIP nanostructuring.[22,41] Further, PSi has been increasingly exploited in optical (bio)sensing with organic bioreceptors,[42–47] thanks to the facile preparation of different optical structures (i.e., interferometers,[42,45,48–50] resonant cavities,[51–53] and waveguides[54–57]), high effective surface for the accommodation of receptors and target molecules (i.e., proteins,[44,45] DNA,[56,58,59] and drugs[60–62]), intrinsic nanoscale filtering that enables operation of PSi sensors with complex biological fluids (i.e., saliva,[46,42] blood,[63,64] and interstitial fluid[65]).

Pyrrole is selected as the functional monomer being already in vapor phase at room temperature[66,67] and widely used in imprinting procedures in liquid-phase on flat surfaces.[68–73] Human hemoglobin (HHb) is chosen as the template molecule considering its significance in biological systems and, in turn, the clinical relevance of its detection for several diseases, including anemia,[74–76] cardiovascular risk,[77–79] and coronary artery disease.[79–81] Besides, the choice of a protein as the template molecule allows demonstrating the robustness of the vapor-phase imprinting procedure on macromolecules, which is intrinsically more challenging than that of small molecules.[5,82–84]

The developed MIP for HHb exhibited high sensitivity, reliability, and reusability for at least one month, along with ability to operate in human plasma.

2. Results and Discussion

The vapor-phase deposition of polypyrrole (PPy) in nanostructured PSi scaffolds was first investigated. As sketched in **Figure 1**a, a nanostructured PSi layer with porosity of ≈72% consisting of vertical pores of ≈32 nm in size (Figure S1, Supporting Information) and 5 µm in length (aspect ratio ≈150) is prepared by two-steps electrochemical etching of a silicon wafer (Figure 1a-1), then oxidized to $PSiO_2$ (Figure 1a-2). The $PSiO_2$ scaffold is exposed to an oxidizing agent, namely $FeCl_3$, so that oxidant molecules are adsorbed on the $PSiO_2$ inner surface (Figure 1a-3). Eventually, PPy deposition on the as-modified $PSiO_2$ scaffold is carried out in an environment saturated with pyrrole vapors (Figure 1a-4). The polymerization process is performed for different times from 1 to 8 h and monitored through UV-vis reflectance spectroscopy. As a benchmark, PPy deposition on $PSiO_2$ scaffolds from liquid-phase was also carried out for the same polymerization times.

Typical reflectance spectra of $PSiO_2$ scaffolds before and after PPy polymerization from vapor and liquid phases are shown in Figure S2a–c (Supporting Information). The reflectance spectrum is attenuated and red-shifted after polymerization, which confirms an increase of the effective refractive index of the porous material and, in turn, the deposition of PPy within the pores. This is further confirmed by the increased fringe contrast in the reflectance spectrum after PPy deposition in the $PSiO_2$ scaffolds. Monitoring of PPy deposition in the porous host versus time is performed measuring changes of the Effective Optical Thickness (EOT = 2nd, with n effective refractive index and d thickness) of the $PSiO_2$ scaffold upon polymerization, calculated by Fourier transform of the reflectance spectrum. Figure 1b summarizes the changes in the EOT value measured after PPy deposition from vapor and liquid phases, using the EOT value of the bare $PSiO_2$ scaffold as reference, namely, EOT-EOT_{PSiO2}. The EOT value of the PPy-coated scaffolds linearly increases with the polymerization time from 1 to 8 h for vapor-phase polymerization. Liquid-phase polymerization up to 5 h results in a similar trend with smaller EOT changes, which indicates that the amount of polymer conformably deposited within the inner surfaces of the pores is smaller; after 8 h a thick PPy layer is visible by naked-eye on top of the $PSiO_2$ scaffold. The latter prevents acquisition of the reflectance spectrum and, in turn, EOT estimation due to strong absorption of PPy thick films in the visible range.[66,85,86] Experimental results in Figure 1b on the deposition of PPy in $PSiO_2$ scaffolds provide a clear indication that the liquid-phase polymerization process is non-uniform over depth within the pores, with the polymerization rate being maximum on the top surface of the scaffold, in agreement with the smaller amount of polymer deposited on the inner surface of the porous scaffold, compared to vapor phase. This is consistent with the diffusion-limited polymerization occurring in liquid phase within nanostructured materials.[87–89]

In vapor phase, the diffusion coefficient of species increases of a factor >1000 with respect to liquid phase, namely, from $\approx 10^{-5}$ to $\approx 10^{-2}$ cm^2 s^{-1},[90] which facilitates the diffusion of monomer

© 2023 The Authors. Small published by Wiley-VCH GmbH

16136829, 2023, 38, Downloaded from https://onlinelibrary.wiley.com/doi/10.1002/smll.202302274 by CochraneItalia, Wiley Online Library on [16/10/2023]. See the Terms and Conditions (https://onlinelibrary.wiley.com/terms-and-conditions) on Wiley Online Library for rules of use; OA articles are governed by the applicable Creative Commons License

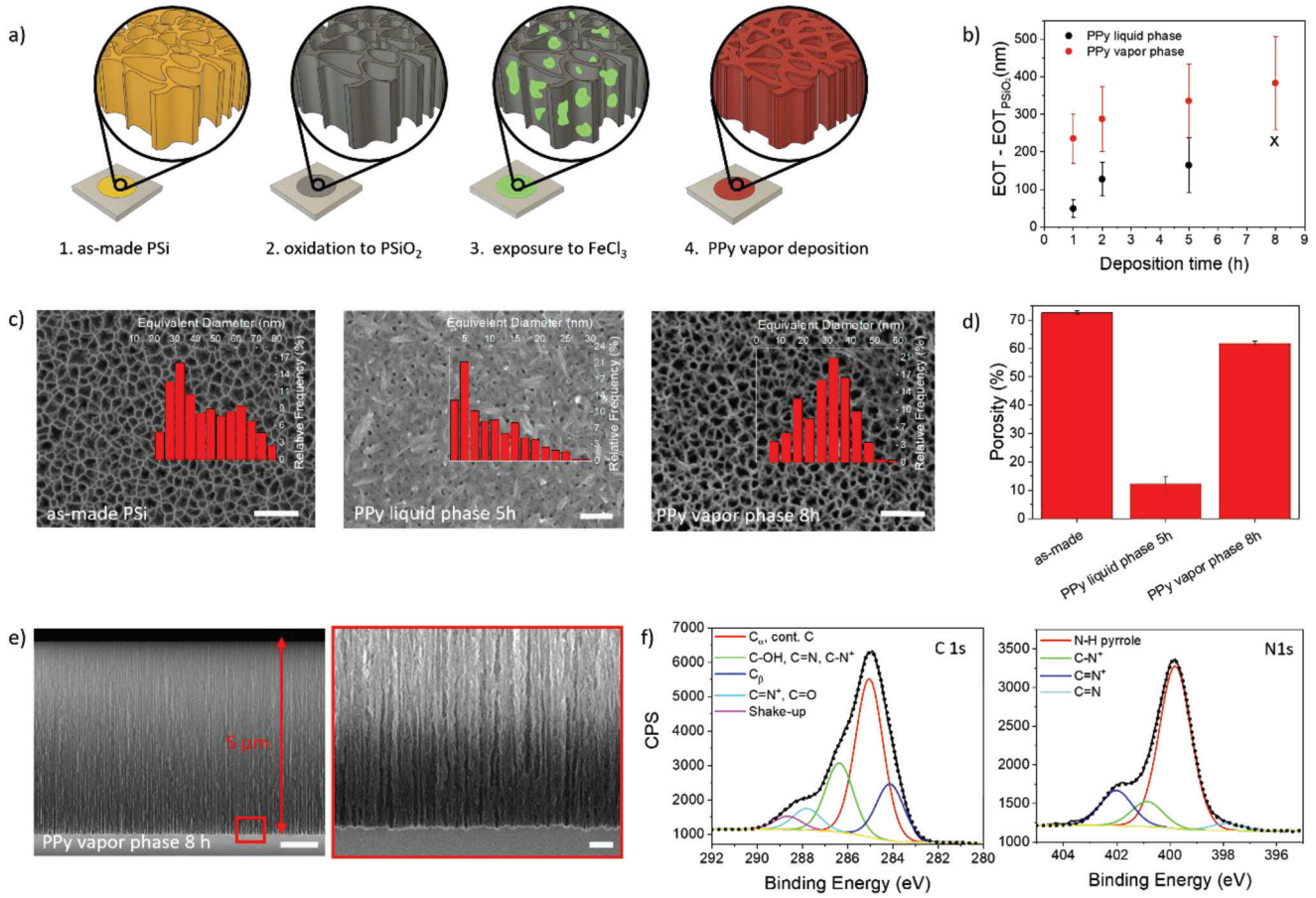

Figure 1. Polypyrrole (PPy) vapor-phase deposition on nanostructured porous silicon oxide ($PSiO_2$) scaffolds. a) Sketch of the vapor-phase polymerization process, starting from as-made PSi (1), which is thermally oxidized to $PSiO_2$ (2), exposed to the oxidizing agent $FeCl_3$ (3), and finally coated with PPy in a chamber saturated with pyrrole vapors (4) for different time intervals. b) Effective optical thickness changes (EOT-EOT_{PSiO2}) of $PSiO_2$ scaffolds coated with PPy through vapor-phase and liquid-phase polymerization, for different time intervals; the EOT value of the bare $PSiO_2$ (EOT_{PSiO2}) scaffold is used as reference (n = 3 samples for each tested time). c) SEM top-view images of as-made PSi and of PPy-coated $PSiO_2$ scaffolds after 5 h liquid-phase polymerization and 8 h vapor-phase polymerization. Insets report pore size distribution. Scale bar is 200 nm. d) Porosity value of the top surface of as-made PSi and PPy-coated $PSiO_2$ scaffolds after 5 h liquid-phase polymerization and 8 h vapor-phase polymerization (n = 3 samples), estimated from SEM top-view images. e) SEM cross-section view images of full thickness (left) and pore bottom (right) of a $PSiO_2$ scaffold after PPy vapor-phase deposition for 8 h. Scale bare is 1 µm (left) and 200 nm (right). f) Detailed C 1s and N 1s XPS signals of PPy deposited on $PSiO_2$ scaffolds by vapor-phase deposition for 8 h. Spectra are fitted and charging corrected. All data are presented as mean (± s.d).

vapors within the nanostructure and, in turn, their adsorption on the nanostructure inner surface, as widely reported for gas diffusion through nanoporous membranes.[91–93] This leads to the vapor-phase deposition of PPy films with higher reliability and uniformity within the $PSiO_2$ scaffolds compared to liquid phase for a given polymerization time, consistently with data shown in Figure 1b. Furthermore, liquid-phase polymerization is prone to the formation of oligomers and (nano)aggregates due to partial dissolution of the oxidant agent upon immersion of the $FeCl_3$-decorated $PSiO_2$ scaffold in the monomer solution. Diffusion of oligomers and (nano)aggregates within the nanopores is further hindered, contributing in preventing polymer deposition on the inner pore surface.[94,95]

Figure 1c shows SEM top-views of $PSiO_2$ scaffolds as-made and coated with PPy for 5 h in liquid phase and 8 h in vapor phase. The scaffold coated with PPy for 8 h in vapor phase closely resembles the as-made scaffold, with similar average size and size distribution of pores (inset in Figure 1c and Figure S1, Supporting Information). A porosity reduction of only 10% is achieved for the 8 h coated scaffold with respect to the as-made scaffold, which corresponds to an average reduction of the pore diameter of ≈4 nm (Figure 1d). These data are consistent with the homogeneous deposition of a few nm-thick polymer on the inner surface of the pores. Conversely, liquid-phase deposition for 5 h leads to the formation of a PPy layer on top of the $PSiO_2$ scaffold with low porosity (10%) almost occluding the pores inlet (Figure 1c,d). This is consistent with the smaller EOT values achieved for liquid-phase PPy polymerization, given that most of the polymer is deposited on top of the $PSiO_2$ scaffold thus reducing the materials coating the inner surface of the pores.

Figure 1e shows a SEM cross-section view of the $PSiO_2$ scaffold after vapor-phase deposition of PPy for 8 h. Columnar pores with same morphology of that of the as-made scaffold are visible (compare Figure 1e; Figure S3b,c, Supporting Information),

© 2023 The Authors. Small published by Wiley-VCH GmbH

16136829, 2023, 38, Downloaded from https://onlinelibrary.wiley.com/doi/10.1002/smll.202302274 by CochraneItalia, Wiley Online Library on [16/10/2023]. See the Terms and Conditions (https://onlinelibrary.wiley.com/terms-and-conditions) on Wiley Online Library for rules of use; OA articles are governed by the applicable Creative Commons License

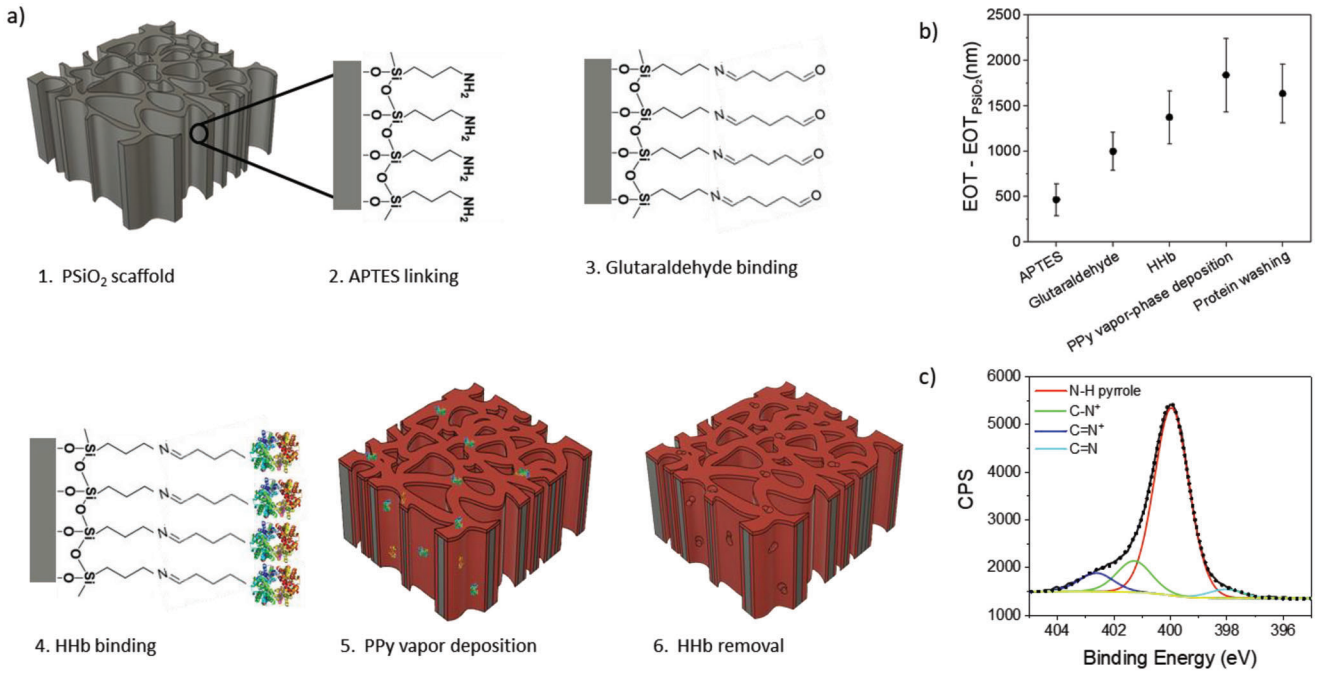

Figure 2. Vapor-phase synthesis of PPy-based molecularly imprinted polymer (MIP) for human hemoglobin (HHb) on $PSiO_2$ scaffold. a) Sketch of the imprinting protocol consisting of (1) preliminary $PSiO_2$ silanization by APTES and (2) linking with glutaraldehyde for (3) HHb coupling, followed by (4) PPy vapor-phase polymerization for 8 h and (5) final washing treatment for HHb removal aiming at obtaining the imprinted cavities within the PPy film. b) Effective optical thickness changes ($EOT\text{-}EOT_{PSiO2}$) achieved for each functionalization step in (a); the EOT value of bare $PSiO_2$ (EOT_{PSiO2}) scaffold is used as reference (n = 3 samples). Data are presented as mean (± s.d.). c) Detailed N 1s XPS signal of MIP for HHb deposited on $PSiO_2$ scaffolds by 8 h vapor-phase polymerization. Signal is fitted and charging corrected.

with no clogging signs over depth. The presence of the polymer in the pores over depth is corroborated by SEM-EDX analyses carried out on the cross-section of $PSiO_2$ scaffolds after PPy deposition (Figure S4, Supporting Information). Nitrogen distribution over the pore depth is selected as the fingerprint of PPy deposition. Figure S4 (Supporting Information) reveals that vapor-phase polymerization for 8 h results in a homogeneous polymer distribution within the porous scaffold. Conversely, a PPy mass decreasing over depth results from EDX analysis after deposition for 5 h in liquid phase.

With the aim of gaining a deeper understanding of vapor-phase deposition of PPy, we carried out XPS analysis of PPy-coated scaffolds prepared under both vapor- and liquid-phase polymerization (Figure 1f; Table S1, Supporting Information). The attenuation of the Si 2p signal upon polymer deposition is indicative of the thickness of the PPy deposited, according to a standard uniform overlayer model[96–98]; the variability of the Si 2p signal over different measurement points gives an indication of the spatial homogeneity of the coating polymer. Upon vapor-phase polymerization a steady increase of the Si 2p signal attenuation is recorded from 1 to 8 h (up to 35%), confirming an increase of the PPy layer thickness that agrees with spectroscopic data in Figure 1b. Conversely, a conspicuous attenuation of the Si 2p signal (97%) is observed already after 5 h of liquid-phase polymerization. This can be ascribed to the formation of a thick PPy film on top of the $PSiO_2$ scaffold, in agreement with SEM data of Figure 1c, which results in a nonuniform polymer deposition within the pores, evidenced by EDX data in Figure S4 (Supporting Information). This is further confirmed by the high variability (percentage relative standard deviation - RSD% - 39.9%) associated with the Si 2p signal on different points of the $PSiO_2$ scaffolds after liquid-phase deposition for 5 h (Table S1, Supporting Information). On the other hand, low variability of the Si 2p signal (RSD% = 3.5%) measured after vapor-phase polymerization for 8 h is consistent with the deposition of a homogeneous PPy film.

Surface chemistry of the PPy film deposited by 8 h vapor-phase synthesis on $PSiO_2$ scaffold is further investigated by XPS analysis. Figure 1f reports fitted spectra of C 1s and N 1s signals. Binding energy and chemical assignment of each component are in good agreement with the literature,[99–101] thus highlighting that the chemical structure of vapor-phase grown PPy on $PSiO_2$ scaffolds is similar to that of PPy deposited on conventional planar substrates from liquid-phase.[100,101] The presence of components at 287.8 eV in C 1s and 402.0 eV in N 1s, assigned to $C{=}N^+$ functionality, reveals that the film is in an oxidized state. This feature is leveraged to promote electrostatic interactions with the template in imprinting procedures.

We next investigated the vapor-phase synthesis of MIP receptors for the protein HHb within the $PSiO_2$ scaffolds. The protocol is sketched in **Figure 2**a. The imprinting procedure leverages the covalent coupling of the target protein HHb to the $PSiO_2$ surface before PPy deposition. HHb anchoring to the $PSiO_2$ surface is carried out through silanization with (3-aminopropyl)triethoxysilane (APTES) to expose amino groups followed by glutaraldehyde binding (Figure 2a1–4). Vapor-phase deposition of PPy for 8 h is then performed as already described (Figure 1a) and eventually HHb is removed through a washing

© 2023 The Authors. Small published by Wiley-VCH GmbH

16136829, 2023, 38, Downloaded from https://onlinelibrary.wiley.com/doi/10.1002/smll.202302274 by CochraneItalia, Wiley Online Library on [16/10/2023]. See the Terms and Conditions (https://onlinelibrary.wiley.com/terms-and-conditions) on Wiley Online Library for rules of use; OA articles are governed by the applicable Creative Commons License

step leaving cavities in the PPy film retaining shape, size, and functionality of the template (Figure 2a5–6). Preliminary anchoring of the template on the nanostructure surface has a twofold advantage: i) only the monomer vaporization is required for promoting polymer deposition; ii) it leads to a stronger imprinting effect thanks to the formation of a higher density and more homogeneous binding site population, compared to polymerization from a monomer-template mixture.[5,102]

Each surface functionalization step is assessed by UV-Vis reflectance spectroscopy, through the acquisition of reflectance spectra and calculation of EOT values (Figure 2b; Figure S5, Supporting Information). A red-shift of the reflectance spectrum is observed after each functionalization step, apart from HHb removal that leads to a blue-shift (Figure S5, Supporting Information). The latter is consistent with the reduction of the effective refractive index of the PPy-coated scaffold after removal of the protein. No significant change in the line-shape of the reflectance spectra is evident, indicating that a uniform coating of the inner pore surface occurs at any step, including PPy deposition. The EOT value steadily increases with respect to the reference value measured on bare $PSiO_2$ scaffolds, except for HHb removal in agreement with the blue shift of the reflectance spectrum.

The EOT change recorded after PPy deposition on the functionalized $PSiO_2$ scaffolds (≈500 nm with respect to the value measured after HHb grafting) is consistent with that measured on non-functionalized scaffolds (Figure 1b), thus indicating that the polymerization process is not affected by the preceding functionalization steps. On the other hand, reduction of the EOT value recorded after HHb washing is comparable with the EOT increase measured after protein grafting, suggesting that the washing step is effective for protein removal from PPy, which is a key requisite for MIP preparation.

We then carried out XPS analysis of MIP-coated $PSiO_2$ scaffolds (Figure 2c; Table S2, Supporting Information). The N 1s spectrum of the MIP is similar to that recorded on PPy (Figure 1f), confirming that vapor-phase polymer deposition is not affected by the presence of HHb on the pore surface. An increase of N–H abundance in the MIP with respect to PPy is observed, reasonably due to aminic functionalities in protein. The slight shift of the binding energy of $C{=}N^+$ groups can be ascribed to the involvement of such PPy functionalities in the interaction with the protein. Remarkably, an atomic ratio N/Si equal to 7.28 is obtained for MIP that is significantly larger than the value of 0.74 achieved for PPy, providing indirect evidence of the successful functionalization of $PSiO_2$ scaffolds.

We eventually performed a series of experiments to assess the sensing performance of MIP-coated $PSiO_2$ scaffolds in detection of HHb (**Figure 3**a), using $PSiO_2$ scaffolds coated with non-imprinted polymer (NIP) as control. Reflectance spectra of MIP- and NIP-coated scaffolds were acquired after exposure to different HHb concentrations in the range 0.1 to 8 mg mL^{-1} (Figure S6, Supporting Information); the change in the EOT value, namely, EOT-EOT_0, was used as the analytical signal, with EOT_0 reference value measured in buffer solution. The range of HHb concentrations is chosen to investigate sensitivity of the MIP in diluted blood samples, which would enable decreasing the sample volume up to a factor 1000, thus strongly reducing medical waste in clinical applications.[76,103–107] Figure 3b shows the calibration curve of the MIP- and NIP-coated $PSiO_2$ scaffolds. Two linear regions are evident for the MIP-based sensor, namely, a higher-sensitivity region between 0.1 and 1 mg mL^{-1} and a lower-sensitivity region between 1 and 8 mg mL^{-1}. The limit of detection estimated from the calibration curve is 0.024 mg mL^{-1}, taking the noise floor of the MIP-coated scaffold in buffer solution into account (LoD = $3.3std_{noise}/S$, with std_{noise} = 0.6 nm and S = 82.5 nm mg^{-1} mL^{-1}). The MIP-based sensor shows an excellent sample-to-sample reproducibility in the low concentration range with RSD% = 1.4% (n = 3). Even considering the entire range, the sensor reproducibility remains satisfactory with RSD% = 16.5%, which highlights a good control of PPy deposition and HHb anchoring/removal procedures.

A high specific interaction of the MIP with the target protein is apparent by comparison of the calibration curves of MIP- and NIP-coated $PSiO_2$ sensors (Figure 3b). The MIP response to HHb is significantly higher than that of the NIP for any of the HHb concentration tested, revealing a highly specific interaction with the protein that is mediated by the strong imprinting effect occurring within the HHb cavities imprinted in PPy. This is quantitatively expressed by the Imprinting Factor (IF), namely, the sensitivity ratio between MIP- and NIP-based sensors. Considering for the MIP sensor an average sensitivity of 44.76 nm mg^{-1} mL^{-1} over the entire concentration range, an IF value of 13.1 is obtained that is comparable with best values reported in the literature for the imprinting of proteins.[5,73] The remarkable imprinting effect is further confirmed by the high selectivity of the MIP-based sensor to HHb against interfering proteins, namely, human serum albumin (HSA), cytochrome C (Cyt C), and lysozyme (Lyz) (Figure 3c). The sensor response to HHb is significantly higher (>30x at the lowest concentration tested) than that measured for the interfering proteins, regardless of molecular weight and concentration. Notice that, HSA has a molecular weight (69 kDa) close to that of HHb (64 kDa), and Lyz (14.5 kDa) and CytC (12.4 kDa) have a much smaller molecular weight that is commonly reported to generate a significant interference response being able to occupy MIP cavities imprinted for larger proteins.[73,108] A slight interference is apparently generated by CytC at high concentrations (interfering ratio equal to 0.26 at 8 mg mL^{-1}). Nonetheless, CytC mean serum levels are significantly lower, ranging from 0.1 to 40 ng mL^{-1},[109] thus not determining any effect on sensor response in real samples.

Effective binding properties of the MIP toward HHb are confirmed by the value of the association constant $K_0 = a^{1/m} = 1.2$ 10^4 M^{-1} we estimated using the Langmuir-Freundlich isotherm model (Figure 3d), in agreement with some literature reports on MIPs.[110,111]

We next assessed the performance of the MIP-based $PSiO_2$ sensor in human plasma and artificial serum spiked with HHb, without further pretreatment (Figure 3d). Plasma and serum provide a complex matrix with composition very similar to blood. Both plasma and serum come from the liquid portion of the blood that remains once the cells are removed, and contain proteins (e.g., serum albumins, globulins, and fibrinogen) and other constituents (e.g., glucose, clotting factors, electrolytes, hormones, carbon dioxide) of whole blood. Figure 3e shows the sensor response to different concentrations of HHb in human plasma and artificial serum, as well as in buffer for comparison. Despite the higher complexity of serum and plasma, a maximum variation of 10% was achieved in the detection of HHb compared

© 2023 The Authors. Small published by Wiley-VCH GmbH

16136829, 2023, 38, Downloaded from https://onlinelibrary.wiley.com/doi/10.1002/smll.202302274 by CochraneItalia, Wiley Online Library on [16/10/2023]. See the Terms and Conditions (https://onlinelibrary.wiley.com/terms-and-conditions) on Wiley Online Library for rules of use; OA articles are governed by the applicable Creative Commons License

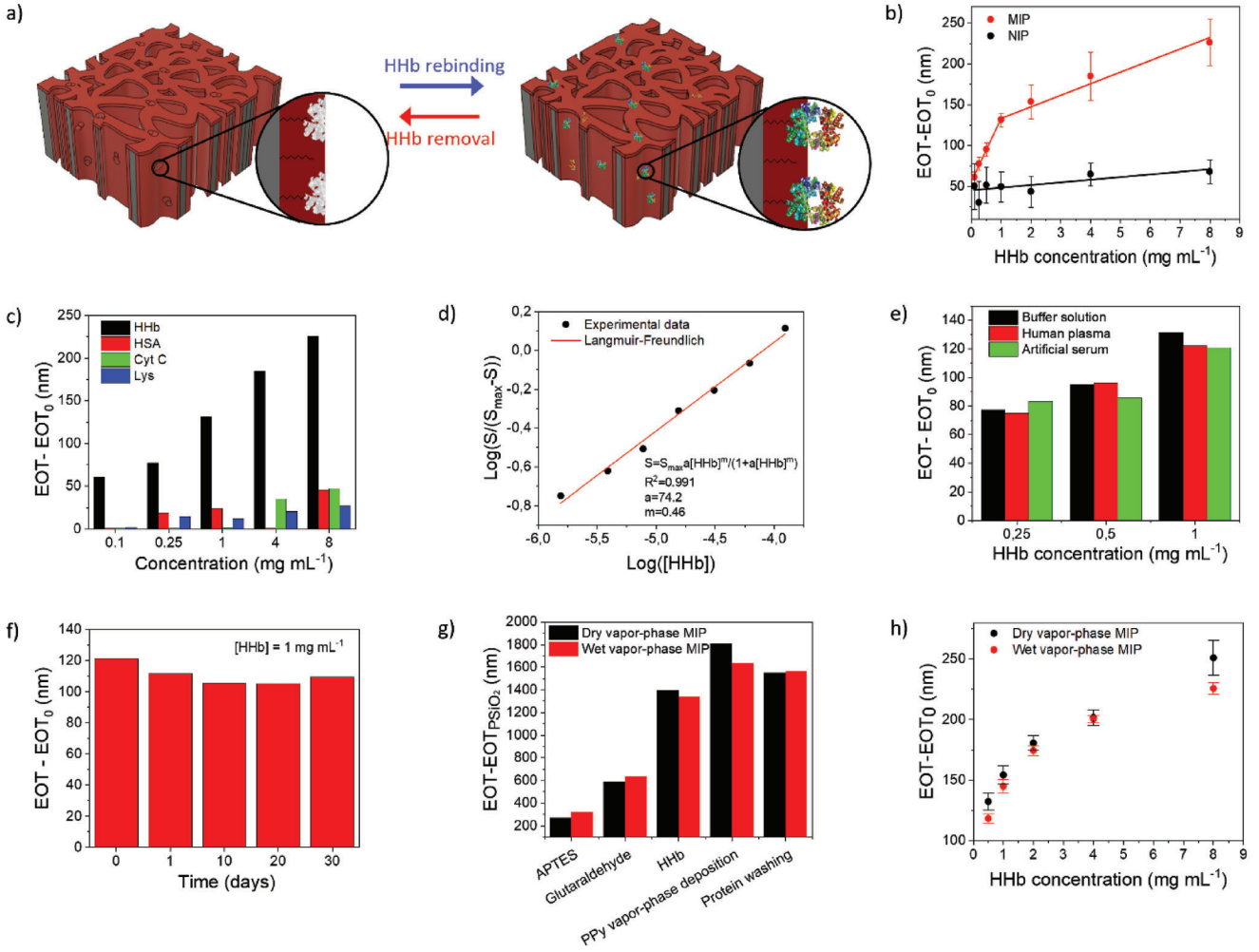

Figure 3. PPy-based MIP sensing performance in HHb optical detection. a) Sketch of target protein interaction with PPy-based MIP on $PSiO_2$ scaffold. b) Calibration curves (EOT-EOT_0 versus HHb concentration) recorded on MIP and not imprinted polymer (NIP) sensors in the range 0.1 to 8 mg mL^{-1}. EOT_0 is measured in buffer solution and used as reference (n = 3 samples). Data are presented as mean (± s.d.). c) Selectivity results comparing the MIP sensor response (calculated as EOT-EOT_0) to HHb with that achieved for interfering proteins, namely, human serum albumin (HSA), cytochrome C (CytC) and lysozyme (Lyz) at different concentrations. d) Best-fitting in log-log scale of the MIP sensor calibration curve in b) (black dots) using the Langmuir-Freundlich isotherm model (red trace), where S = EOT-EOT_0 is the sensor output. Fitting parameters are S_{max} = 400 nm maximum value of the sensor output, a = 74.2 related to the median binding affinity, and m = 0.46 heterogeneity index. Experimental data are presented as the mean value of n = 3 samples. e) MIP sensor response (calculated as EOT-EOT_0) in real samples of human plasma and artificial serum spiked with HHb at different concentrations. f) MIP sensor response (calculated as EOT-EOT_0) versus time measured over 30 days at HHb concentration of 1 mg mL^{-1}. g,h) Comparison of room-temperature vapor-phase synthesis (g) and sensing performance (h) of PPy-based MIP for human hemoglobin (HHb) prepared in $PSiO_2$ scaffolds in dry and wet conditions. Effective optical thickness changes (EOT-EOT_{PSiO2}) achieved for each functionalization step (g). Calibration curves (EOT-EOT_0 versus HHb concentration) recorded in the range 0.5 to 8 mg mL^{-1} for vapor-phase MIP deposited in dry and wet conditions (h). EOT_0 is measured in buffer solution and used as reference (n = 3 measures). Data are presented as mean (± s.d.).

to buffer, thus demonstrating the suitability of the MIP-based $PSiO_2$ sensor to operate with whole biological fluids in real settings.

The sensing performance of the MIP toward HHb provides indirect evidence that the protein retained its structure during the vapor-phase polymerization of PPy, given that the MIP specifically rebinds HHb in buffer solution and serum/plasma samples, where the protein is expected to maintain its natural structure. Thus, it cannot be a-priori excluded that the protein has maintained a certain degree of hydration within the nanopores, which might be compatible with the gentle drying process of the porous scaffold after exposure to the protein solution and before exposure to pyrrole vapors.

We then performed an additional set of experiments to verify that the vapor-phase pyrrole polymerization in the nanoporous silica scaffold–and, in turn, on other substrates–can be also carried out in the presence of saturated water vapors (wet vapor-phase deposition) in the evaporation chamber, thus ensuring hydration–and preventing denaturation–of biomolecules used as the template over the whole polymerization time. Wet vapor-phase deposition of PPy was carried out at room temperature and atmospheric pressure by placing a small amount of water

© 2023 The Authors. Small published by Wiley-VCH GmbH

16136829, 2023, 38, Downloaded from https://onlinelibrary.wiley.com/doi/10.1002/smll.202302274 by CochraneItalia, Wiley Online Library on [16/10/2023]. See the Terms and Conditions (https://onlinelibrary.wiley.com/terms-and-conditions) on Wiley Online Library for rules of use; OA articles are governed by the applicable Creative Commons License

in the evaporation chamber together with pyrrole. Control experiments of PPy deposition by vapor phase in absence of water were carried out as usual (and referred as dry vapor-phase). No significant differences were found in wet and dry conditions in terms of material thickness and sensing performance toward HHb (Figure 3g,h). The possibility of carrying out the vapor-phase MIP deposition in the presence of saturated water vapors significantly extends the use of the proposed strategy to a large assortment of biomolecules, further supported by the mild conditions employed in both MIP synthesis and rebinding steps, not involving any organic solvents (which would seriously limit the application to biomolecules) nor any light-temperature input for triggering polymerization, contrarily to other imprinting strategies applied to nanostructures.[26,31,32]

Eventually, we tested reusability and aging of the MIP-coated $PSiO_2$ sensor by monitoring the response to HHb at 1 mg mL^{-1} over 30 days (Figure 3e). No particular care was taken for the sensor storage, which was kept at room temperature in ambient air. The sensor was reused five times over 30 days and the response remained stable over multiple measurements, with an average variability of 11.4% over one month. Regeneration of the sensor is obtained by simply washing the MIP in acidic solution for HHb removal, thus demonstrating that the sensor can be stored after fabrication before use, then easily reused multiple times.

3. Conclusions

Here, we reported on a novel route that leverages vapor-phase polymerization for the synthesis of MIPs on nanostructured materials. PPy was selected as the polymer due to monomer vaporization at room temperature and wide use in molecular imprinting strategies; nanostructured $PSiO_2$ was chosen as the target substrate to demonstrate improved reliability and homogeneity of PPy and MIP deposition on high aspect-ratio nanomaterials by vapor phase, with respect to liquid-phase polymerization. The MIP was imprinted for HHb and exhibited high sensitivity, selectivity, and stability over time in the detection of the target protein, leveraging the $PSiO_2$ nanomaterial as the optical transducer.

The proposed vapor-phase strategy overcomes well-known limitations of the liquid-phase synthesis in the control of polymer and MIP film deposition in nanostructures, and paves the way towards the use of MIP synthetic receptors in difficult-to-coat nanomaterials. Further, it is immediately extendable to other target analytes and nanomaterials/transducers taking advantage of the substrate-independent deposition mechanism.

Supporting Information

Supporting Information is available from the Wiley Online Library or from the author.

Acknowledgements

This work was partially funded by the European Union Horizon Europe programme under grant agreement No 101046946 (RESORB).

Conflict of Interest

The authors declare no conflict of interest.

Data Availability Statement

The data that support the findings of this study are available in the supplementary material of this article.

Keywords

molecularly imprinted polymers, optical sensors, porous silicon, protein detection, synthetic receptors, vapor-phase polymerization

Received: March 17, 2023
Revised: April 27, 2023
Published online: May 24, 2023

[1] B. T. S. Bui, K. Haupt, *Anal. Bioanal. Chem.* **2010**, *398*, 2481.
[2] M. Cieplak, W. Kutner, *Trends Biotechnol.* **2016**, *34*, 922.
[3] J. Wackerlig, P. A. Lieberzeit, *Sens Actuators B Chem* **2015**, *207 (Part A)*, 144.
[4] O. S. Ahmad, T. S. Bedwell, C. Esen, A. Garcia-Cruz, S. A. Piletsky, *Trends Biotechnol.* **2019**, *3*, 294.
[5] E. Mazzotta, T. Di Giulio, C. Malitesta, Electrochemical Sensing of Macromolecules Based on Molecularly Imprinted Polymers: Challenges, Successful Strategies, and Opportunities. **2022**, *414*, 5165.
[6] A. Chiappini, L. Pasquardini, A. M. Bossi, *Sensors* **2020**, *20*, 5069.
[7] K. Haupt, P. X. Medina Rangel, B. T. S. Bui, *Chem. Rev.* **2020**, *120*, 9554.
[8] K. Haupt, K. Mosbach, *Trends Biotechnol.* **1998**, *16*, 468.
[9] K. Haupt, *Chem. Commun. (Camb)*. **2003**, *2*, 171.
[10] E. Mazzotta, T. Di Giulio, C. Malitesta, *Anal. Bioanal. Chem.* **2022**. 5165, https://doi.org/10.1007/S00216-022-03981-0.
[11] T. Di Giulio, E. Mazzotta, C. Malitesta, *Biosensors* **2020**, *11*, 3.
[12] T. Di Giulio, A. Barca, T. Verri, M. De Gennaro, G. Giancane, E. Mazzotta, C. Malitesta, *Sens Actuators B Chem* **2023**, 133589. https://doi.org/10.1016/J.SNB.2023.133589.
[13] A. Herrera-Chacón, X. Cetó, M. Del Valle, *Anal. Bioanal. Chem.* **2021**, *413*, 6117.
[14] R. D'Aurelio, I. Chianella, J. A. Goode, I. E. Tothill, *Biosensors* **2020**, *10*, https://doi.org/10.3390/bios10030022.
[15] T. Kamra, S. Chaudhary, C. Xu, L. Montelius, J. Schnadt, L. Ye, *J. Colloid Interface Sci.* **2016**, *461*, https://doi.org/10.1016/j.jcis.2015.09.009.
[16] U. Arshad, A. Mujahid, P. Lieberzeit, A. Afzal, S. Z. Bajwa, N. Iqbal, S. Roshan, *RSC Adv.* **2020**, *10*, 34355.
[17] R. Gui, H. Guo, H. Jin, *Nanoscale Adv* **2019**, *1*, 3325.
[18] C. Unger, P. A. Lieberzeit, *React. Funct. Polym.* **2021**, *161*, 104855.
[19] A. M. Gavrilă, E. B. Stoica, T. V. Iordache, A. Sârbu, *Appl. Sci.* **2022**, *12*, 3080.
[20] X. Qiu, X. Y. Xu, Y. Liang, Y. Hua, H. Guo, *J. Chromatogr. A* **2016**, *1429*, 79.
[21] X. Qiu, X. Y. Xu, Y. Liang, H. Guo, *Food Chem.* **2018**, *258*, 295.
[22] A. V. Linares, A. Falcimaigne-Cordin, L. A. Gheber, K. Haupt, *Small* **2011**, *7*, 2318.
[23] E. Paruli, O. Soppera, K. Haupt, C. Gonzato, *ACS Appl Polym Mater* **2021**, *3*, 4769.
[24] R. Batul, T. Tamanna, A. Khaliq, A. Yu, *Biomater. Sci.* **2017**, *5*, 1204.
[25] Y. Liu, L. Liu, Y. He, Q. He, H. Ma, *Biosens. Bioelectron.* **2016**, *77*, 886.
[26] M. J. Garcia-Soto, K. Haupt, C. Gonzato, *Polym. Chem.* **2017**, *8*, 4830.
[27] S. Patra, E. Roy, R. Madhuri, P. K. Sharma, *Biosens. Bioelectron.* **2015**, *66*, https://doi.org/10.1016/j.bios.2014.10.076.
[28] H. Y. Lee, B. S. Kim, *Biosens. Bioelectron.* **2009**, *25*, 587.

© 2023 The Authors. Small published by Wiley-VCH GmbH

16136829, 2023, 38, Downloaded from https://onlinelibrary.wiley.com/doi/10.1002/smll.202302274 by CochraneItalia, Wiley Online Library on [16/10/2023]. See the Terms and Conditions (https://onlinelibrary.wiley.com/terms-and-conditions) on Wiley Online Library for rules of use; OA articles are governed by the applicable Creative Commons License

[29] M. Hu, P. Huang, L. Suo, F. Wu, *Microchim. Acta* **2018**, *185*, https://doi.org/10.1007/s00604-018-2826-2.
[30] M. Zhang, X. Zhang, X. He, L. Chen, Y. Zhang, *Nanoscale* **2012**, *4*, 3141.
[31] S. Subrahmanyam, A. Guerreiro, A. Poma, E. Moczko, E. Piletska, S. Piletsky, *Eur. Polym. J.* **2013**, *49*, 100.
[32] A. R. Guerreiro, I. Chianella, E. Piletska, M. J. Whitcombe, S. A. Piletsky, *Biosens. Bioelectron.* **2009**, *24*, 2740.
[33] G. O. Ince, E. Armagan, H. Erdogan, F. Buyukserin, L. Uzun, G. Demirel, *ACS Appl. Mater. Interfaces* **2013**, *5*, 6447.
[34] R. Xing, Y. Wen, Y. Dong, Y. Wang, Q. Zhang, Z. Liu, *Anal. Chem.* **2019**, *91*, 9993.
[35] R. Xing, Z. Guo, H. Lu, Q. Zhang, Z. Liu, *Sci. Bull.* **2022**, *67*, 278.
[36] Z. Guo, R. Xing, M. Zhao, Y. Li, H. Lu, Z. Liu, *Adv. Sci.* **2021**, *8*, 2101713.
[37] F. A. Harraz, M. S. Salem, T. Sakka, Y. H. Ogata, *Electrochim. Acta* **2008**, *53*, 3734.
[38] F. A. Harraz, *J. Electrochem. Soc.* **2006**, *153*, C349.
[39] Z. Chen, V. Robbiano, G. M. Paternò, G. Carnicella, A. Debrassi, A. A. La Mattina, S. Mariani, A. Minotto, G. Egri, L. Dähne, F. Cacialli, G. Barillaro, *Adv. Opt. Mater.* **2021**, *9*, 2100036.
[40] C. S. Peyratout, L. Dähne, *Angew. Chem., Int. Ed.* **2004**, *43*, 3762.
[41] Z. Zhang, S. Xu, J. Li, H. Xiong, H. Peng, L. Chen, *J. Agric. Food Chem.* **2012**, *60*, 180.
[42] S. Mariani, V. Robbiano, L. M. Strambini, A. Debrassi, G. Egri, L. Dähne, G. Barillaro, *Nat. Commun.* **2018**, *9*, https://doi.org/10.1038/s41467-018-07723-8.
[43] M. Corsi, A. Paghi, S. Mariani, G. Golinelli, A. Debrassi, G. Egri, G. Leo, E. Vandini, A. Vilella, L. Dähne, D. Giuliani, G. Barillaro, *Adv. Sci.* **2022**, *2202062*, 2202062.
[44] S. Mariani, L. Pino, L. M. Strambini, L. Tedeschi, G. Barillaro, *ACS Sens.* **2016**, *1*, 1471.
[45] S. Mariani, L. M. Strambini, G. Barillaro, *Anal. Chem.* **2016**, *88*, 8502.
[46] S. Mariani, A. Paghi, A. A. La Mattina, A. Debrassi, L. Dähne, G. Barillaro, *ACS Appl. Mater. Interfaces* **2019**, *11*, 43731.
[47] A. Jane, R. Dronov, A. Hodges, N. H. Voelcker, *Trends Biotechnol.* **2009**, *27*, 230.
[48] A. Paghi, L. Strambini, F. F. Toia, M. Sambi, M. Marchesi, R. Depetro, M. Morelli, G. Barillaro, *Adv. Electron. Mater.* **2020**, *6*, http://dx.doi.org/10.1002/aelm.202000615.
[49] V. S. Y. Lin, K. Motesharei, K. P. S. Dancil, M. J. Sailor, M. R. Ghadiri, *Science (80-)* **1997**, *278*, 840.
[50] D. N. Kumar, N. Pinker, G. Shtenberg, *ACS Sens.* **2020**, *5*, 1969.
[51] L. De Stefano, I. Rea, I. Rendina, L. Rotiroti, M. Rossi, S. D'Auria, *Phys. status solidi* **2006**, *203*, 886.
[52] V. Robbiano, G. M. Paternò, A. A. La Mattina, S. G. Motti, G. Lanzani, F. Scotognella, G. Barillaro, *ACS Nano* **2018**, *12*, 4536.
[53] B. Sciacca, F. Frascella, A. Venturello, P. Rivolo, E. Descrovi, F. Giorgis, F. Geobaldo, *Sens Actuators B Chem* **2009**, *137*, 467.
[54] C. A. Barrios, S. Carrasco, M. Francesca, P. Yurrita, F. Navarro-Villoslada, M. C. Moreno-Bondi, *Sens Actuators B Chem* **2012**, *161*, 607.
[55] A. Loni, L. T. Canham, M. G. Berger, R. Arens-Fischer, H. Munder, H. Luth, H. F. Arrand, T. M. Benson, *Thin Solid Films* **1996**, *276*, 143.
[56] G. Rong, J. D. Ryckman, R. L. Mernaugh, S. M. Weiss, *Appl. Phys. Lett.* **2008**, *93*, 161109.
[57] S. A. Rinne, F. García-Santamaría, P. V. Braun, *Nat. Photonics* **2008**, *2*, 52.
[58] C. Pacholski, *Sensors* **2013**, *13*, 4694.
[59] G. Di Francia, V. La Ferrara, S. Manzo, S. Chiavarini, *Biosens. Bioelectron.* **2005**, *21*, 661.
[60] M. P. Stewart, J. M. Buriak, *Adv. Mater.* **2000**, *12*, 859.
[61] L. M. Bonanno, L. A. DeLouise, *Anal. Chem.* **2010**, *82*, 714.
[62] T. Guinan, M. Ronci, H. Kobus, N. H. Voelcker, *Talanta* **2012**, *99*, 791.
[63] S. Dhanekar, S. Jain, *Biosens. Bioelectron.* **2013**, *41*, 54.
[64] M. Terracciano, I. Rea, N. Borbone, R. Moretta, G. Oliviero, G. Piccialli, L. De Stefano, *Mol.* **2019**, *24*, 2216.
[65] C. Chiappini, in *Porous Silicon for Biomedical Applications*, Woodhead Publishing, Helsinki, Finland **2021**, pp. 545–570.https://doi.org/10.1016/B978-0-12-821677-4.00006-9.
[66] J. Kim, D. Sohn, Y. Sung, E. R. Kim, *Synth. Met.* **2003**, *132*, 309.
[67] H. Niu, H. Zhou, H. Wang, T. Lin, H. Niu, H. Zhou, H. Wang, T. Lin, *Macromol. Mater. Eng.* **2016**, *301*, 707.
[68] A. Turco, S. Corvaglia, E. Mazzotta, *Biosens. Bioelectron.* **2015**, *63*, 240.
[69] M. Díaz-Álvarez, E. Mazzotta, C. Malitesta, A. Martín-Esteban, *J. Mol. Recognit.* **2014**, *27*, 415.
[70] N. Ktari, N. Fourati, C. Zerrouki, M. Ruan, M. Seydou, F. Barbaut, F. Nal, N. Yaakoubi, M. M. Chehimi, R. Kalfat, *RSC Adv.* **2015**, *5*, 88666.
[71] V. Ratautaite, R. Boguzaite, E. Brazys, A. Ramanaviciene, E. Ciplys, M. Juozapaitis, R. Slibinskas, M. Bechelany, A. Ramanavicius, *Electrochim. Acta* **2022**, *403*, 139581.
[72] B. Schweiger, J. Kim, Y. J. Kim, M. Ulbricht, *Sensors (Basel)*. **2015**, *15*, 4870.
[73] J. Erdòssy, V. Horváth, A. Yarman, F. W. Scheller, R. E. Gyurcsányi, *Trends Analyt Chem* **2016**, *79*, 179.
[74] R. Fitzsimmons, N. Amin, V. N. Uversky, Understanding the Roles of Intrinsic Disorder in Subunits of Hemoglobin and the Disease Process of Sickle Cell Anemia. **2016**, *4* e1248273. https://doi.org/10.1080/21690707.2016.1248273.
[75] D. J. Schaer, P. W. Buehler, A. I. Alayash, J. D. Belcher, G. M. Vercellotti, *Blood* **2013**, *121*, 1276.
[76] H. H. Billett, in *Clinical Methods: The History, Physical, and Laboratory Examinations*, Eds. H. Walker, W. Hall, J. Hurst, Butterworths, Boston **1990**, pp. 763–763.
[77] G. Lee, S. Choi, K. Kim, J. M. Yun, J. S. Son, S. M. Jeong, S. M. Kim, S. M. Park, *J Am Heart Assoc* **2018**, *7*. https://doi.org/10.1161/JAHA.117.007723.
[78] T. Shimakawa, D. E. Bild, *J Clin Epidemiol* **1993**, *46*, 1257.
[79] K. T. Khaw, N. Wareham, *Curr. Opin. Lipidol.* **2006**, *17*, 637.
[80] M. Chonchol, C. Nielson, Hemoglobin Levels and Coronary Artery Disease. **2008**, *155*, 494–498.
[81] D. E. Houghton, I. Koh, A. Ellis, N. S. Key, D. R. Douce, G. Howard, M. Cushman, M. Safford, N. A. Zakai, *Am J Hematol* **2020**, *95*, 258.
[82] Y. Saylan, F. Yilmaz, E. Özgür, A. Derazshamshir, H. Yavuz, A. Denizli, *Sensors (Basel)*. **2017**, *17*. https://doi.org/10.3390/S17040898
[83] S. Li, S. Cao, M. J. Whitcombe, S. A. Piletsky, *Prog. Polym. Sci.* **2014**, *39*, 145.
[84] M. Trojanowicz, In *Combinatorial Methods for Chemical and Biological Sensors*, Eds. R. A. Potyrailo, V. M. Mirsky, Springer Verlag, New York, USA **2009**, 52. https://doi.org/10.1007/978-0-387-73713-3.
[85] X. Chen, N. Yu, L. Zhang, Z. Liu, Z. Wang, Z. Chen, *RSC Adv.* **2015**, *5*, 96888.
[86] O. Niwa, M. Hikita, T. Tamamura, *Appl. Phys. Lett.* **1998**, *46*, 444.
[87] J. S. Andrew, E. J. Anglin, E. C. Wu, M. Y. Chen, L. Cheng, W. R. Freeman, M. J. Sailor, *Adv. Funct. Mater.* **2010**, *20*, 4168.
[88] M. Y. Chen, M. J. Sailor, *Anal. Chem.* **2011**, *83*, 7186.
[89] Y. Yong, X. Lou, S. Li, C. Yang, X. Yin, *Comput. Math. with Appl.* **2014**, *67*, 412.
[90] J. Marc, S. R. M. Madou, *Chemical Sensing with Solid State Devices* **1989**. https://doi.org/10.1016/c2009-0-22258-6.
[91] S. Mohammed, A. K. Sunkara, C. E. Walike, G. Gadikota, *Front. Clim.* **2021**, *3*. https://doi.org/10.3389/fclim.2021.713708.
[92] K. Wu, X. Li, C. Wang, W. Yu, Z. Chen, *Ind. Eng. Chem. Res.* **2015**, *54*, 3225.

© 2023 The Authors. Small published by Wiley-VCH GmbH

16136829, 2023, 38, Downloaded from https://onlinelibrary.wiley.com/doi/10.1002/smll.202302274 by CochraneItalia, Wiley Online Library on [16/10/2023]. See the Terms and Conditions (https://onlinelibrary.wiley.com/terms-and-conditions) on Wiley Online Library for rules of use; OA articles are governed by the applicable Creative Commons License

[93] S. Y. Yoo, J. S. Roh, J. Kim, W. Kim, H. B. Park, H. W. Kim, *ACS Appl. Nano Mater.* **2022**, *5*, 7029.
[94] J. Jiang, L. Zhu, L. Zhu, B. Zhu, Y. Xu, *Langmuir* **2011**, *27*, 14180.
[95] Y. Ding, L.-T. Weng, M. Yang, Z. Yang, X. Lu, N. Huang, Y. Leng, *Langmuir* **2014**, *30*, 12258.
[96] A. G. Shard, *J. Vac. Sci. Technol. A Vacuum, Surfaces, Film.* **2020**, *38*, 041201.
[97] M. A. Isaacs, J. Davies-Jones, P. R. Davies, S. Guan, R. Lee, D. J. Morgan, R. Palgrave, *Mater. Chem. Front.* **2021**, *5*, 7931.
[98] A. G. Shard, S. J. Spencer, *Surf. Interface Anal.* **2017**, *49*, 1256.
[99] C. Malitesta, I. Losito, L. Sabbatini, P. G. Zambonin, *J Electron Spectros Relat Phenomena* **1995**, *76 (C)*, 629.
[100] E. De Giglio, M. R. Guascito, L. Sabbatini, G. Zambonin, *Biomaterials* **2001**, *22*, 2609.
[101] E. De Giglio, L. Sabbatini, P. G. Zambonin, *J Biomater Sci Polym Ed* **2012**, *10*, 845.
[102] T. Di Giulio, E. Mazzotta, C. Malitesta, *Biosens* **2020**, *11*, 3.
[103] J. T. Kuenstner, K. H. Norris, W. F. McCarthy, *Appl. Spectrosc.* **1994**, *48*, 484.
[104] M. Rendell, E. Anderson, W. Schlueter, J. Mailliard, D. Honigs, R. Rosenthal, *Clin. Lab. Haematol.* **2003**, *25*, 93.
[105] T. Bodley, M. Chan, L. Clarfield, O. Levi, A. Longmore, W. Lin, D. Yip, S. Orla, J. O. Friedrich, L. K. Hicks, *Blood* **2019**, *134*, 57.
[106] A. Shander, H. L. Corwin, *Transfus Med Rev* **2020**, *34*, 195.
[107] M. L. Compton, P. C. Szklarski, G. S. Booth, *Arch Pathol Lab Med* **2018**, *142*, 358.
[108] E. Verheyen, J. P. Schillemans, M. Van Wijk, M. A. Demeniex, W. E. Hennink, C. F. Van Nostrum, *Biomaterials* **2011**, *32*, 3008.
[109] T. Eleftheriadis, G. Pissas, V. Liakopoulos, *Front Immunol* **2016**, *7*, 279.
[110] R. J. Umpleby, S. C. Baxter, Y. Chen, R. N. Shah, K. D. Shimizu, *Anal. Chem.* **2001**, *73*, 4584.
[111] R. J. Ansell, In *Advances in Biochemical Engineering/Biotechnology*, Springer Science and Business Media Deutschland GmbH, Cham, Germany **2015**, *150*, 51–93.

© 2023 The Authors. Small published by Wiley-VCH GmbH

16136829, 2023, 38, Downloaded from https://onlinelibrary.wiley.com/doi/10.1002/smll.202302274 by CochraneItalia, Wiley Online Library on [16/10/2023]. See the Terms and Conditions (https://onlinelibrary.wiley.com/terms-and-conditions) on Wiley Online Library for rules of use; OA articles are governed by the applicable Creative Commons License